

Atomic-scale studies of garnet-type $\text{Mg}_3\text{Fe}_2\text{Si}_3\text{O}_{12}$: Defect chemistry, diffusion and dopant properties

Kuganathan, N & Chroneos, A

Published PDF deposited in Coventry University's Repository

Original citation:

Kuganathan, N & Chroneos, A 2020, 'Atomic-scale studies of garnet-type $\text{Mg}_3\text{Fe}_2\text{Si}_3\text{O}_{12}$: Defect chemistry, diffusion and dopant properties', *Journal of Power Sources Advances*, vol. 3, 100016.

<https://dx.doi.org/10.1016/j.powera.2020.100016>

DOI 10.1016/j.powera.2020.100016

ISSN 2666-2485

Publisher: Elsevier

This is an open access article under the CC BY license

(<http://creativecommons.org/licenses/by/4.0/>). *Journal of Power Sources Advances* 3 (2020) 100016

Copyright © and Moral Rights are retained by the author(s) and/ or other copyright owners. A copy can be downloaded for personal non-commercial research or study, without prior permission or charge. This item cannot be reproduced or quoted extensively from without first obtaining permission in writing from the copyright holder(s). The content must not be changed in any way or sold commercially in any format or medium without the formal permission of the copyright holders.



Atomic-scale studies of garnet-type $\text{Mg}_3\text{Fe}_2\text{Si}_3\text{O}_{12}$: Defect chemistry, diffusion and dopant properties

Navaratnarajah Kuganathan^{a,b,*}, Alexander Chroneos^{a,b}

^a Department of Materials, Imperial College London, London, SW7 2AZ, United Kingdom

^b Faculty of Engineering, Environment and Computing, Coventry University, Priory Street, Coventry, CV1 5FB, United Kingdom

ARTICLE INFO

Keywords:

Defects
Diffusion
 $\text{Mg}_3\text{Fe}_2\text{Si}_3\text{O}_{12}$
Dopants
Atomistic simulation

ABSTRACT

Materials with low cost, environmentally benign, high structural stability and high Mg content are of considerable interest for the construction of rechargeable Mg-ion batteries. In the present study, atomistic simulations are used to provide insights into defect and diffusion properties of garnet type $\text{Mg}_3\text{Fe}_2\text{Si}_3\text{O}_{12}$. Calculations reveal that the Mg–Fe anti-site defect cluster (0.44 eV/defect) is the lowest energy intrinsic defect process. Three dimensional Mg-ion migration pathway with the activation energy of 2.19 eV suggests that Mg-ion diffusion in this material is slow. Favourable isovalent dopants are found to be Mn^{2+} , Ga^{3+} and Ge^{4+} on the Mg, Fe and Si sites respectively. While the formation of Mg interstitials required for the capacity is facilitated by Al doping on the Si site, Mg vacancies needed for the vacancy assisted Mg-ion diffusion are enhanced by Ge doping on the Fe site. The electronic structures of favourable dopants are calculated and discussed using density functional theory.

1. Introduction

The continued depletion of fossil fuel resources has led to the research activity to find alternative energy storage systems such as batteries and fuel cells. Rechargeable Li-ion battery is currently being considered as a potential energy source for many portable electronic devices [1–5]. As the global demand for large scale applications such as electrical vehicles increases rapidly, battery systems based on other monovalent cations such as Na^+ [6,7] or divalent cations such as Mg^{2+} [8], Ca^{2+} [9] and Zn^{2+} [10] are being considered as alternatives to Li-ion batteries. Batteries based on divalent cations are expected to provide high energy density for large-scale applications as they can undergo beyond one-electron redox reactions.

Mg-ion batteries are of considerable interest for the next generation of energy storage due to low cost, high energy density and high safety [11–14]. However, the intercalation of Mg^{2+} ions in the electrode materials is expected to be difficult due to the strong ionic interaction between Mg^{2+} ions and the host lattices. This problem is now being partly resolved by synthesizing electrode materials at the nano-scale [15] and reducing the shielding of Mg^{2+} ions in the lattice [16]. A limited number of electrode materials including MgFeSiO_4 [17], MgMn_2O_4 [18], Mg_6MnO_8 [19], V_2O_5 [20] and MnO_2 [21] have been so far examined.

Naturally occurring minerals have been considered for potential

application as electrode materials in Mg and Ca-ion batteries [19,22–24]. Recently MgFeSiO_4 which belongs to olivine-type mineral was examined as a promising cathode material for Mg-ion batteries [23]. Mg-based rock-forming silicate garnet $\text{Mg}_3\text{Fe}_2\text{Si}_3\text{O}_{12}$ [25] is a candidate material for assessing its suitability as an electrode material for numerous reasons. This material consists of three Mg ions per formula unit and $(\text{SiO}_4)^{4-}$ units offering structural stability via strong Si–O bonds. Furthermore, silicon and iron are relatively safe, abundant and cheap. To the best of our knowledge, $\text{Mg}_3\text{Fe}_2\text{Si}_3\text{O}_{12}$ was not studied either experimentally or theoretically to examine the defect, dopant, transport and electronic properties.

As defect and transport properties of $\text{Mg}_3\text{Fe}_2\text{Si}_3\text{O}_{12}$ are of greater importance in assessing its suitability in batteries, in this study, computer modelling based on the interatomic potentials is carried out using established lattice energy minimisation technique to provide information about the lattice properties, defect formation energies, Mg-ion diffusion pathways and solution of dopants. This method has been successfully applied to a wide range of energy materials [26–29]. Additionally, density functional theory (DFT) based energy minimisation techniques was applied to investigate the electronic structures of doped configurations.

* Corresponding author. Department of Materials, Imperial College London, London, SW7 2AZ, United Kingdom.

E-mail addresses: n.kuganathan@imperial.ac.uk (N. Kuganathan), ad0636@coventry.ac.uk (A. Chroneos).

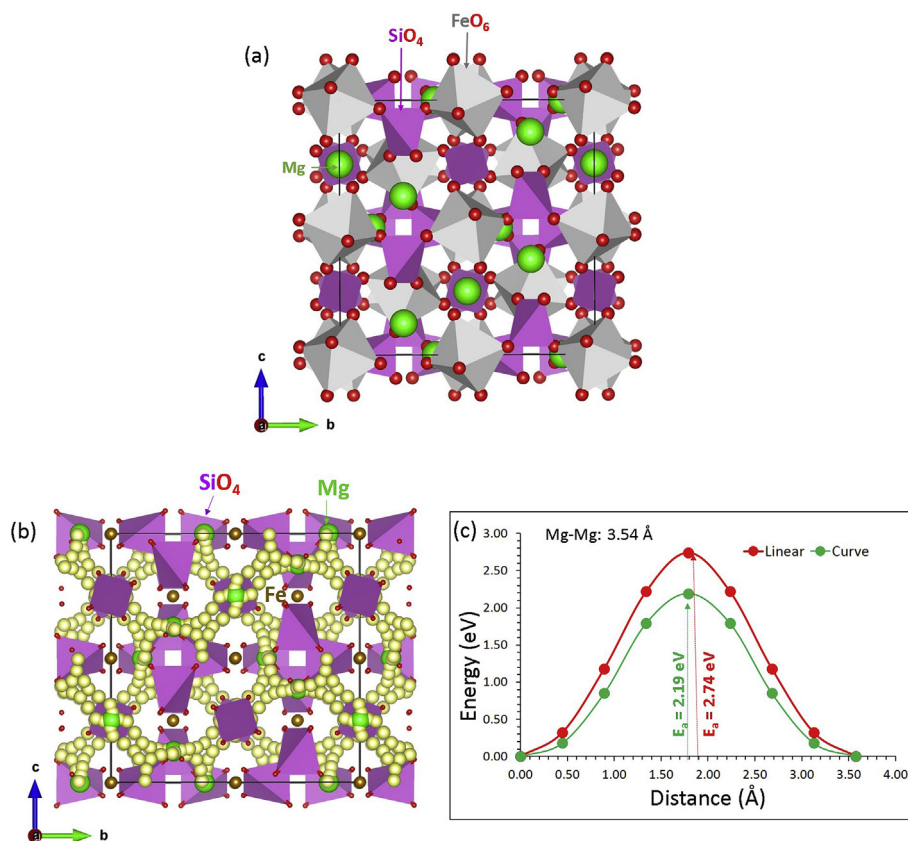


Fig. 1. (a) Crystal structure of $\text{Mg}_3\text{Fe}_2\text{Si}_3\text{O}_{12}$, (b) long range Mg-ion diffusion path and (c) energy profile diagram showing the activation energies calculated for linear (direct) and non-linear (curve) pathways.

2. Computational methods

Defect calculations were performed using a well-established classical simulation code GULP (General Utility Lattice Program) [30]. This code uses the Born model description of an ionic crystal lattice. Lattice energy is defined as the sum of long-range attractive forces (Coulomb) and short-range forces [repulsive (Pauli) and attractive (van der Waals)]. Buckingham potentials were used to model the short range interactions. Ionic positions and lattice parameters were relaxed using the Broyden-Fletcher-Goldfarb-Shanno (BFGS) algorithm as implemented in the GULP code [31]. All defect calculations were performed with a supercell consisting of 704 atoms. Point defects were modelled using the Mott-Littleton method [32]. Two adjacent Mg vacancy sites were considered as initial and final configurations for the migration of Mg-ion. Activation energy was defined as the energy difference between the vacancy formation energy and the maximum energy along the diffusion path. As defects are at dilute limit with full charge, there will be an overestimation in the defect enthalpies. However, relative energies and trends will be consistent. From a thermodynamical point of view, the defect parameters (i.e. formation energies) can be defined

via the comparison of the defective (real) crystal to an isobaric (or isochoric) non-defective (ideal) crystal. These defect formation parameters are interconnected through thermodynamic relations as outlined in previous studies [33,34]. In this study, calculations correspond to the isobaric parameters for the migration and formation processes [35,36].

Electronic structure calculations were performed using a plane wave DFT code VASP (Vienna Ab initio Simulation Package) [37]. This code uses plane wave basis sets and PAW (Projected Augment Wave) pseudo-potentials [38]. A plane wave basis set with a cut-off of 500 eV was used in all calculations. Exchange-correlation effects were treated using generalized gradient approximation (GGA) as implemented by Perdew, Burke and Ernzerhof (PBE) [39]. The conjugate gradient (CG)

Table 1

Calculated and experimental lattice parameters of cubic $\text{Mg}_3\text{Fe}_2\text{Si}_3\text{O}_{12}$.

Parameter	Calculated		Experiment [25]	Δ (%)	
	Force field	DFT		Force field	DFT
$a = b = c =$ (Å)	11.6743	11.5600	11.6900	0.13	1.11
$\alpha = \beta = \gamma$ (°)	90.00	90.00	90.00	0.00	0.00
V (Å ³)	1591.0769	1543.6429	1597.5098	0.40	3.37

algorithm was used to minimize the energy. A supercell containing 160 atoms was used. The force tolerance was less than 0.001 eV/Å in all relaxed configurations. A $2 \times 2 \times 2$ Monkhorst Pack k -point mesh [40] which yielded 8 k -points was used. Short range dispersive attractive interactions were modelled using DFT + D3 method implemented by Grimme et al. [41].

3. Results and discussion

3.1. Crystal structure of $\text{Mg}_3\text{Fe}_2\text{Si}_3\text{O}_{12}$

$\text{Mg}_2\text{Fe}_2\text{Si}_3\text{O}_{12}$ belongs to the garnet-type and crystallises in the cubic space group $Ia\bar{3}d$ (no. 230) with the lattice parameters $a = b = c = 11.69$ Å, $\alpha = \beta = \gamma = 90^\circ$ and $V = 1597.51$ Å³ [25]. The Mg^{2+} ion forms 8-fold coordination with adjacent oxygens. Octahedral (FeO_6) and tetrahedral (SiO_4) units share their corners and form a three-dimensional network as shown in Fig. 1a. Energy minimisation calculations were performed to test the suitability of the classical pair potentials, pseudopotentials and basis sets used in this study. Table 1 reports the experimental and calculated lattice parameters, showing the

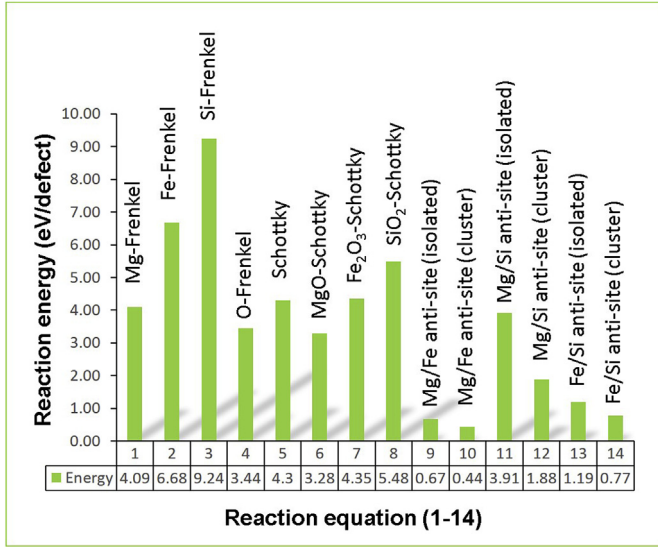


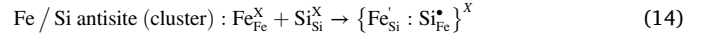
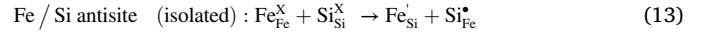
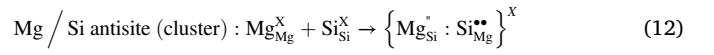
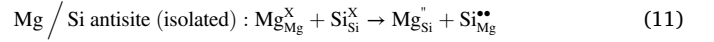
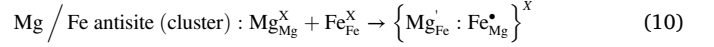
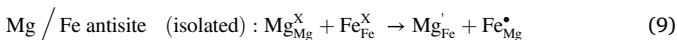
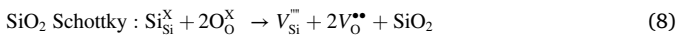
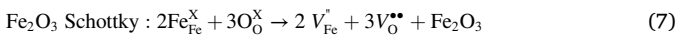
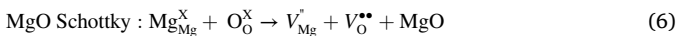
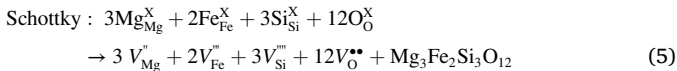
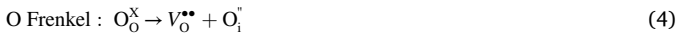
Fig. 2. Reaction energies for different defect processes.

good agreement and supporting the validity of the parameters used in this study.

The calculated maximum specific capacity of $\text{Mg}_3\text{Fe}_2\text{Si}_3\text{O}_{12}$ is 349 mAhg^{-1} (see supplementary information for the calculation formula used) inferring the importance of this material for future application magnesium ion batteries. However, practical difficulties do not allow to provide maximum specific capacity and the real quantity should be calculated from the experiments.

3.2. Energetics of intrinsic defect processes

Classical simulations were applied to gain insight into the formation of point defects and key defect processes such as Schottky, Frenkel and anti-site. These defect processes are important as they can influence the electrochemical properties of $\text{Mg}_3\text{Fe}_2\text{Si}_3\text{O}_{12}$. The point defects (vacancies and interstitials) were combined to calculate Schottky and Frenkel defect formation energies. In order to write complete Schottky reaction equations (eqs (6)–(8)), appropriate lattice energies were calculated (refer to Table S3 for lattice phases together with their lattice energy per formula). The following equations as written using Kröger-Vink notation [42] describe those defect processes in detail.



In Fig. 2, we report the calculated reaction energies per defect for all processes. The lowest energy defect process is for the Mg–Fe anti-site defect cluster. Other anti-site defect cluster energies are also calculated to be low. This indicates a small amount of cation mixing can be found in this material. Many experimental and theoretical studies identified this defect at different experimental conditions and during cycling the batteries [43–45]. Schottky disorder is a process in which charge-balancing populations of vacancies are created and then displaced to the surface of the crystal (equation (5)). Among other defect processes, the MgO–Schottky is the lowest energy process with the defect energy of 3.28 eV/defect. This process will enhance the formation of $\text{V}_{\text{Mg}}^{\bullet\bullet}$ and $\text{V}_{\text{O}}^{\bullet\bullet}$ at high temperatures. The oxygen and magnesium Frenkel energies are calculated to be 3.44 eV/defect and 4.09 eV/defect respectively and they differ by 1 eV from the MgO–Schottky ensuring the possibility of MgO loss in this material at high temperatures. The Fe Frenkel, Si Frenkel and SiO_2 Schottky energies are highly endothermic suggesting that they will not be present at significant concentrations.

3.3. Diffusion of Mg-ions

In this section, we discuss the diffusion of Mg^{2+} ions in order to assess the suitability of this material as a cathode in Mg-ion batteries. Performance of a battery is partly dependent on the materials with high ionic conductivity. Slow diffusion will degrade the battery performance during the intercalation. As diffusion depends on the crystal structure, examining diffusion pathways together with activation energies in $\text{Mg}_3\text{Fe}_2\text{Si}_3\text{O}_{12}$ is necessary. Here we use classical simulation to calculate the vacancy assisted migration of Mg^{2+} ions. In a previous study [46], this methodology has proven to be efficient. For example, there was an excellent agreement between the calculated Li-ion migration pathway and that observed in the neutron diffraction experiment in LiFePO_4 [46, 47].

We identified a potential Mg–Mg hop with the jump distance of 3.54 Å. Importantly, this hop is connected to form a three-dimensional long-range migration path as shown in Fig. 1b. Activation energies calculated for linear and curved pathways are 2.78 eV and 2.19 eV respectively (refer to Fig. 1c). In the linear pathway, Mg^{2+} ions migrate in a straight line and this pathway does not guarantee the lowest activation energy. We allowed the migration ion in different directions as described in our [26,28,29] and previous simulations [27,47] to attain the lowest

Table 2

Mg-based materials and their activation energies for Mg-ion migration.

Material	Activation energy (eV)
MgFeSiO ₄	0.60 [25]
MgV ₂ O ₄	0.52 [48]
MgTiO ₃	0.88 [49]
Mg ₆ MnO ₈	0.82 [50]
MgCr ₂ O ₄	0.69 [51]
MgMn ₂ O ₄	0.40 [52]
MgTa ₂ O ₆	2.21 [53]

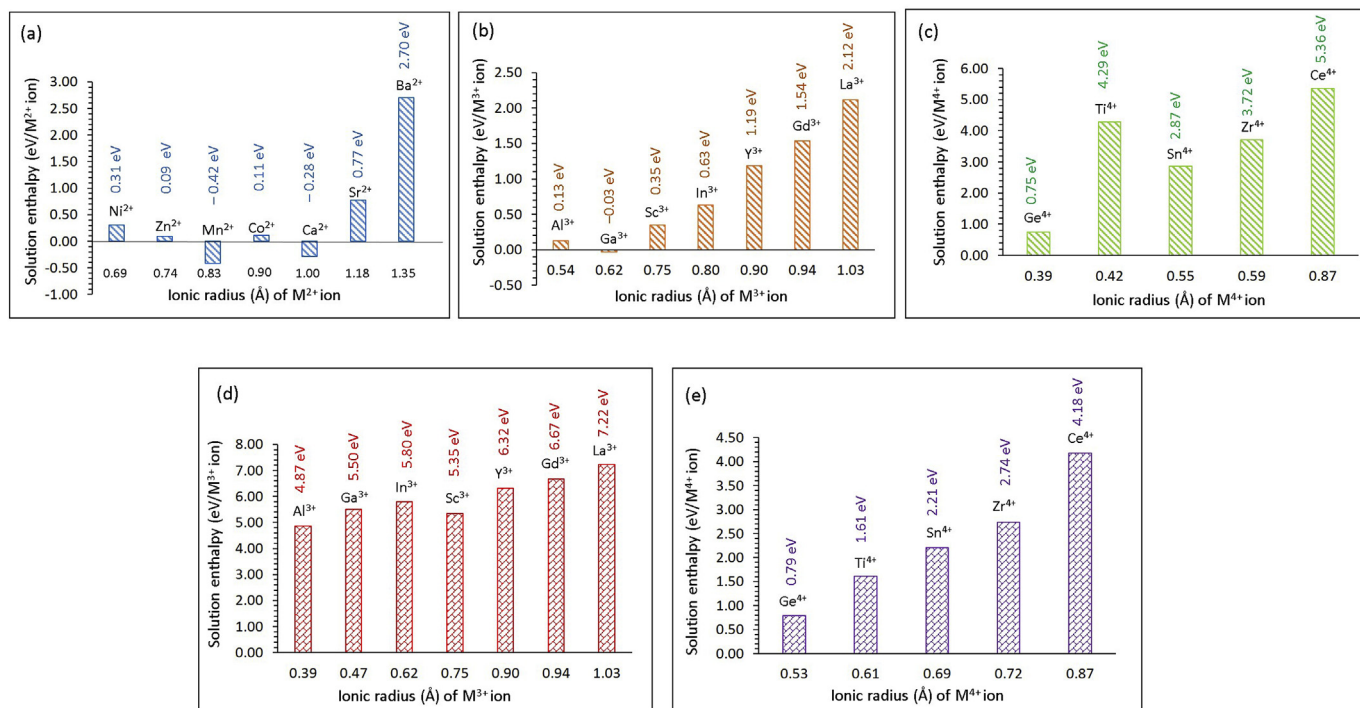


Fig. 3. Enthalpy of solution as a function of dopant radius for (a) divalent cations on the Ca site, (b) trivalent cations on the Fe site, (c) tetravalent cations on the Si, (d) trivalent cations on the Si site for the formation of Ca interstitials and (e) tetravalent cations on the Fe site for the formation of Mg vacancies.

migration energy pathway. We noticed that activation energy calculated for the linear pathway is higher in energy by 0.59 eV than that calculated for the curved pathway. A long Mg–Mg hop distance of 5.46 Å was also identified. However, this yielded a high activation energy of 4.89 eV. The activation energy calculated for the Mg₃Fe₂Si₃O₁₂ shows that the Mg-ion diffusion is slow in this material. A probable solution to increase the ion diffusion can be shorten the Mg–Mg distance in this material. This can be achieved by synthesizing nanoparticles or doping appropriate cations via introducing additional Mg²⁺ ions in the lattice. Previous simulations considered Mg-based materials for use in Mg-ion batteries and their activation energies for Mg-ion migration are tabulated in Table 2 [23, 48–53]. Recent DFT simulation study considered a variety of Ca based minerals and it is shown that garnet type Ca₃Cr₂Si₃O₁₂ and Ca₃Mn₂Si₃O₁₂ materials exhibit three-dimensional Ca-ion migration transport with activation energies of 2.07 eV and 2.09 eV respectively [24]. Activation energy calculated for Ca-ion migration in a similar garnet type structure Ca₃Mn₂Si₃O₁₂ is closer to the value calculated for Mg-ion migration in Mg₃Fe₂Si₃O₁₂ suggesting that there is a strong electrostatic interaction present between migrating cations and the other ions in the lattice.

3.4. Solution of dopants

Substitution of suitable dopants is an effective way of stabilizing a material in order to prevent unfavourable transformations and enhance its electronic properties. The most favourable dopants can be of interest in the experimental investigations to tune the properties of Mg₃Fe₂Si₃O₁₂. A wide range of cations were substituted and their solution energies were calculated. Appropriate charge compensating defects and lattice energies were combined to construct the defect equations. The results are discussed in terms of solution energy, cation size and local environment of dopant atoms. Buckingham potentials used for dopants are given in the electronic supplementary information (ESI) (refer to Table S1). Formulae used to calculate defect energies and solution energies are given in the ESI (refer to Table S2). Table S3 in the ESI provides the information of lattice phases considered together with lattice

energies per formula unit. Bond distances and bond angles calculated around the favourable dopants using DFT and classical simulations were in good agreement with a strong validation of the results.

3.4.1. Divalent dopants

First we considered the substitution of divalent cations (M = Ni, Zn, Mn, Co, Ca, Sr and Ba) on the Mg site. The following reaction equation describes the doping mechanism in which there is no charge compensation. The calculated solution energies are shown in Fig. 3a.



The lowest solution enthalpy (-0.42 eV), and therefore highest solubility, is predicted for Mn²⁺. The negative solution enthalpy suggests that Mn²⁺ would be a promising stabilizing agent. Notably, the solution enthalpy for Ca²⁺ is also negative (-0.28 eV) meaning that it can also be tested experimentally. A very low endoergic solution enthalpy of ~0.10 eV is calculated for Zn²⁺ and Co²⁺ suggesting that these two dopants are also candidates to be tested but would require a small amount of energy in the form of heat. The ionic radius of Mg²⁺ in an eight coordination environment is 0.89 Å. Favourability of these four dopants can be due to their ionic radii (between 0.74 Å and 1.00 Å) which are close to the ionic radius of Mg²⁺ ion. A small ionic radius difference (0.20 Å) between Ni²⁺ and Mg²⁺ results a slightly high endoergic (0.31 eV) solution enthalpy. Solution enthalpy increases with ionic radius from Sr²⁺ (0.77 eV) to Ba²⁺ (2.70 eV). The highest solution enthalpy calculated for Ba²⁺ suggests this dopant is very unfavourable on the Mg site.

3.4.2. Trivalent dopants

Thereafter, we considered a range of trivalent cations (M = Al, Ga, In, Sc, Y, Gd and La) on the Fe and Si sites. Substitution on the Fe site does not require any point defects to charge compensation because of the +3 charge on the Fe in Mg₃Fe₂Si₃O₁₂ (refer to equation (16)). Solution enthalpies are plotted as a function of dopant size in Fig. 3b.



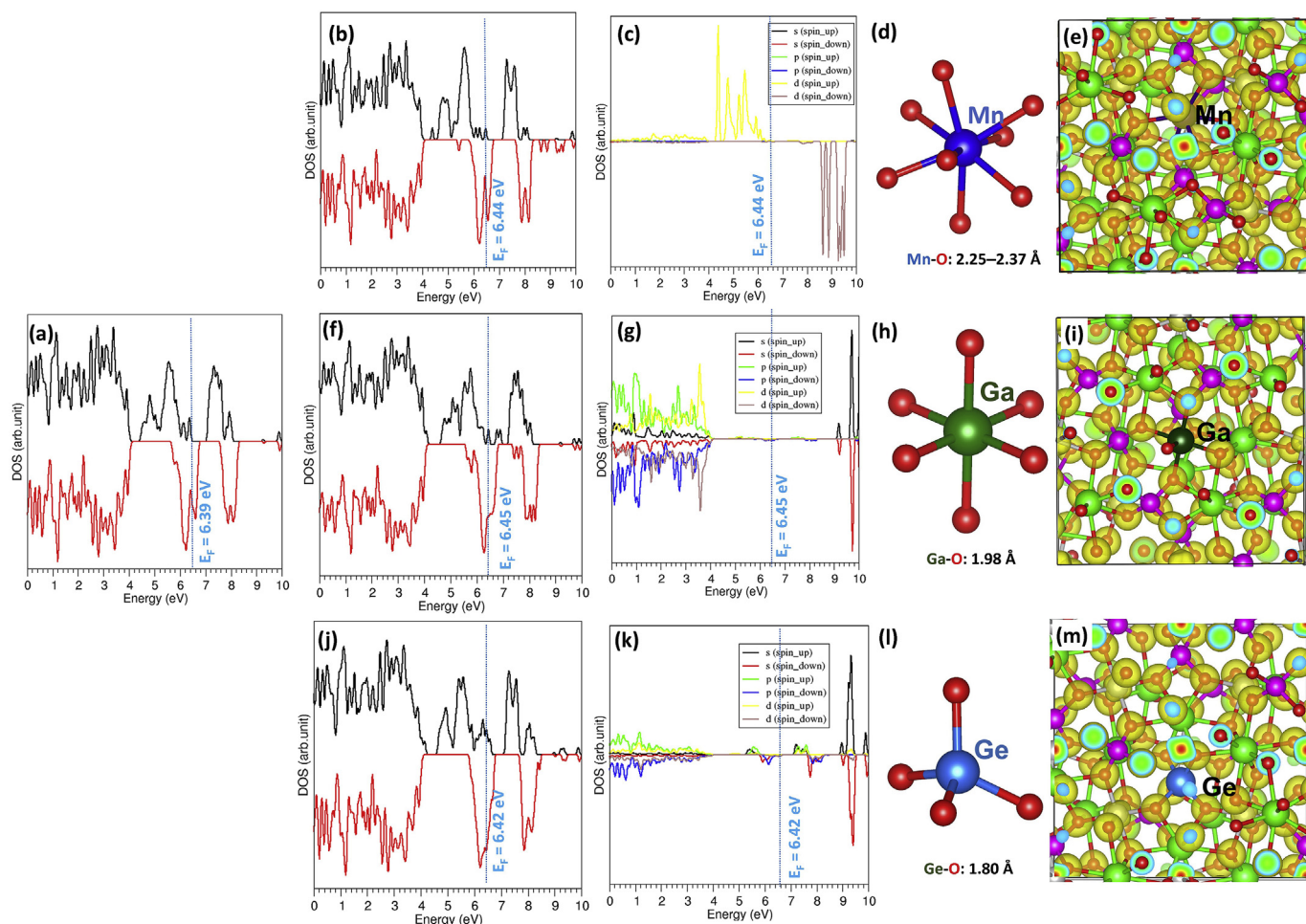
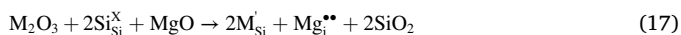


Fig. 4. (a) DOS plot of bulk $\text{Mg}_3\text{Fe}_2\text{Si}_3\text{O}_{12}$ (b) DOS plot of Mn-doped $\text{Mg}_3\text{Fe}_2\text{Si}_3\text{O}_{12}$ (c) atomic DOS plot of Mn (d) optimised MnO_8 unit with bond distance (e) constant charge density plot of Mn-doped $\text{Mg}_3\text{Fe}_2\text{Si}_3\text{O}_{12}$ (f) DOS plot of Ga-doped $\text{Mg}_3\text{Fe}_2\text{Si}_3\text{O}_{12}$ (g) atomic DOS plot of Ga (h) optimised GaO_6 unit with bond distance (i) constant charge density plot of Ga-doped $\text{Mg}_3\text{Fe}_2\text{Si}_3\text{O}_{12}$ (j) DOS plot of Ge-doped $\text{Mg}_3\text{Fe}_2\text{Si}_3\text{O}_{12}$ (k) atomic DOS plot of Ge (l) optimised GeO_4 unit with bond distance and (m) constant charge density plot of Ge-doped $\text{Mg}_3\text{Fe}_2\text{Si}_3\text{O}_{12}$.

The most favourable dopant is calculated to be Ga^{3+} with the exothermic solution enthalpy of -0.03 eV. This can be due to the ionic radius of Fe^{3+} (0.65 Å) closer to that of Ga^{3+} (0.62 Å). The second most favourable dopant is Al^{3+} and its solution enthalpy is 0.13 eV. Solution enthalpy increases with the ionic radius from Sc^{3+} to La^{3+} . The highest solution enthalpy is calculated for La^{3+} (ionic radius 1.03 Å) meaning that La doping is unfavourable.

The Si site was also considered for doping to create additional Mg^{2+} ions as charge compensating defects in this material (refer to equation (17) in what follows). This defect mechanism can be an efficient way of increasing the concentration of Mg in $\text{Mg}_3\text{Fe}_2\text{Si}_3\text{O}_{12}$ in order to increase its capacity. In a previous experimental study, Co^{3+} was doped on the Ru site in Li_2RuO_3 and it was shown that doping enhanced the electrochemical reversibility of Li^+ ions and the amount of Li^+ in the lattice [54].



In Fig. 3d, we report the solution enthalpies for this defect mechanism. In all cases solution enthalpies are highly positive (>4.50 eV) showing the inefficacy of this process. However, the most favourable dopant Al^{3+} might be worth trying experimentally. The lowest solution enthalpy for Al^{3+} can be due to the small difference in their ionic radii. High endothermic process for this mechanism can be due to the high defect formation energy of quadruply charged Si.

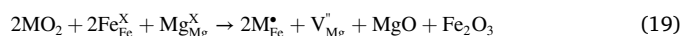
3.4.3. Tetravalent dopants

Finally tetravalent dopants ($\text{M} = \text{Ge}, \text{Ti}, \text{Sn}, \text{Zr}$ and Ce) were considered for the substitution on the Si and Fe sites. Solution enthalpies calculated for the substitution on the Si site are reported in Fig. 3c. The following defect equation explains the mechanism involved in this process.



The results show that the most favourable solution energy (0.75 eV) is predicted for Ge^{4+} . This is due to a small ionic radius difference between Ge^{4+} (0.39 Å) and Si^{4+} (0.26 Å). The solution enthalpy for Ti^{4+} is calculated to be 4.29 eV meaning that it is an unfavourable dopant. The second favourable dopant is Sn^{4+} with the solution enthalpy of 2.87 eV. Solution enthalpy gradually increases with increasing ionic radius. The highest enthalpy of solution for Ce^{4+} (5.36 eV) suggests that doping would require external heat energy.

The formation of Mg vacancies required for the vacancy assisted Mg-ion migration was considered by doping tetravalent cations on the Fe site:



Calculated energies of solution are reported in Fig. 3e. Germanium is identified as a promising dopant for this process as it has the lowest solution enthalpy of 0.79 eV. Solution enthalpy gradually increases with

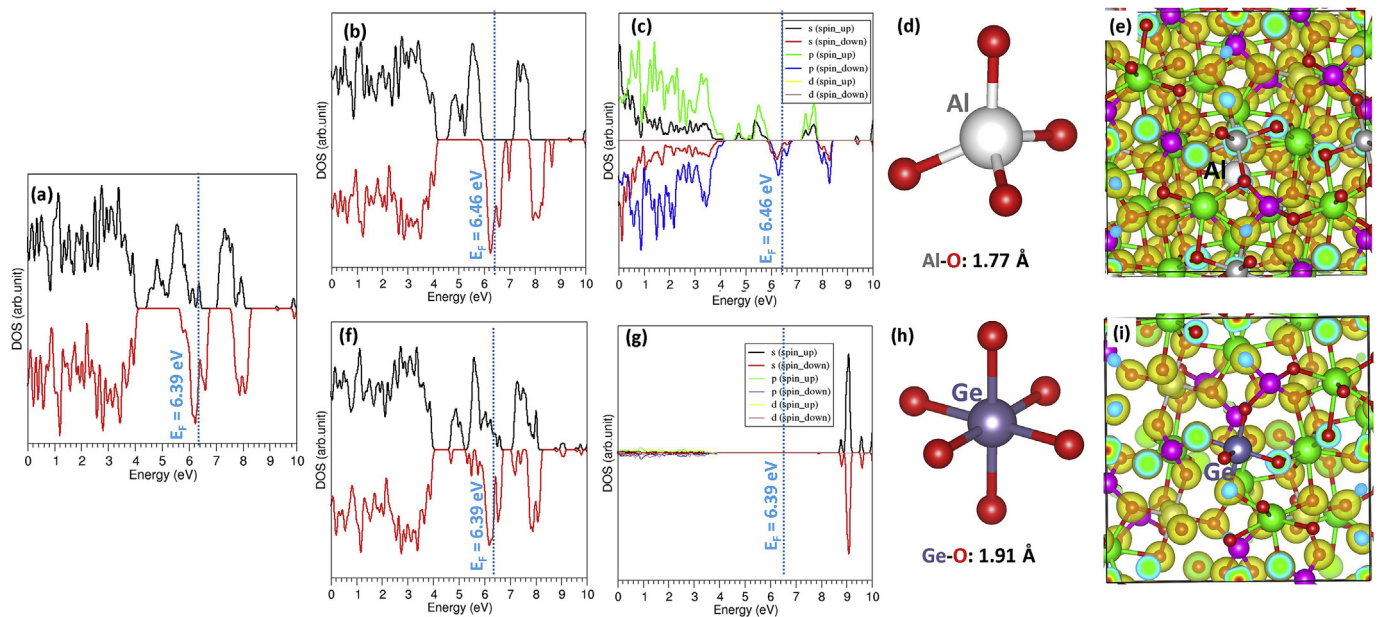


Fig. 5. (a) DOS plot of bulk $\text{Mg}_3\text{Fe}_2\text{Si}_3\text{O}_{12}$, (b) DOS plot of Al-doped $\text{Mg}_3\text{Fe}_2\text{Si}_3\text{O}_{12}$, (c) atomic DOS plot of Al (d) optimised AlO_4 unit with bond distance, (e) constant charge density plot of Al-doped $\text{Mg}_3\text{Fe}_2\text{Si}_3\text{O}_{12}$, (f) DOS plot of Ge-doped $\text{Mg}_3\text{Fe}_2\text{Si}_3\text{O}_{12}$ (g) atomic DOS plot of Ge (h) optimised GeO_4 unit with bond distance (i) constant charge density plot of Ge-doped $\text{Mg}_3\text{Fe}_2\text{Si}_3\text{O}_{12}$.

ionic radius and the highest positive enthalpy value is noted for Ce^{4+} meaning that doping is unlikely to occur at normal temperatures.

3.5. Mg-ion diffusion in the presence of dopants

Here we calculate the activation energies for Mg-ion diffusion in the presence of Al^{3+} on the Si site, Ge^{4+} on the Si site and Ga^{3+} on the Fe site. Energy profile diagrams for the local Mg hop are shown in the ESI (refer to Fig. S1). There is a reduction (by 0.07 eV) in the activation energy for the doping of Al^{3+} on the Si site. In the case of doping of Ge^{4+} on the Si site, activation energy is reduced by 0.09 eV. Doping of Ga^{3+} on the Fe site results a reduction in the activation energy by 0.11 eV. In all cases, Mg-Mg distances have been slightly altered compared to the distances present in the un-doped crystal structure. This perturbation in the distances are due to the charge or ionic radius mismatch between Al^{3+} and Si^{4+} , Ge^{4+} and Si^{4+} and Ga^{3+} and Fe^{3+} . Current simulation shows that doping of Al^{3+} and Si site would simultaneously increase the concentration of Mg^{2+} ions in the lattice and slightly reduces the activation energy of the Mg-ion migration.

3.6. Electronic structure of doped $\text{Mg}_3\text{Fe}_2\text{Si}_3\text{O}_{12}$

Here we use DFT simulations to examine the electronic structures of doped configurations and discuss the results calculated for the most favourable dopants (Mn^{2+} , Ga^{3+} , Al^{3+} and Ge^{4+}) as discussed in section 3.4.

The DOS plot calculated for bulk $\text{Mg}_3\text{Fe}_2\text{Si}_3\text{O}_{12}$ is shown in Fig. 4a. It is shown that the ferromagnetic configuration of bulk $\text{Mg}_3\text{Fe}_2\text{Si}_3\text{O}_{12}$ exhibits metallic behaviour. Doping Mn does not alter the electronic structure much as shown in the DOS plot (refer to Fig. 4b). Peaks associated with the 3d states of Mn appear near the Fermi level (refer to Fig. 4c). Calculated Mn-O bond distances (2.25 Å–2.37 Å) are larger than the Mg-O (1.922 Å–1.944 Å) bond distances though the ionic radii of Mg^{2+} and Mn^{2+} are close to each other. The deviation can be due to the fact that the Mn has greater shielding than the Mg. Constant charge density plot of Mn-doped configuration is shown in Fig. 4e.

In the case of Ga, the Fermi level is slightly altered but maintaining metallic behaviour (refer to Fig. 4f). There is no significant contribution to the DOS plot from Ga near the Fermi level. States associated with Ga

appear in the conduction band (refer to Fig. 4g). Ga-O bond distances are longer only by ~ 0.05 Å than the Fe-O bond distances (1.92 Å–1.94 Å). This is due to a very small difference in their ionic radii.

Doping Ge on the Si site has only a minor effect on the DOS plot (refer to Fig. 4j). The doped configuration is metallic. A very small peak that belongs to 3s and 3p states of Ge appear just below the Fermi level (refer to Fig. 4k). The Si-O bond distance in the undoped $\text{Mg}_3\text{Fe}_2\text{Si}_3\text{O}_{12}$ is 1.65 Å. The Ge-O bond distance is longer than (by 0.15 Å) than the Si-O bond distance. This is due to the larger ionic radius of Ge^{4+} (0.39 Å) than that of Si^{4+} (0.26 Å).

Doping Al on the Si site shifts the Fermi energy level only by 0.07 eV (refer to Fig. 5b). The doped configuration is metallic. Additional peaks arising from 3s and 3p states of Al appear near the Fermi level (refer to Fig. 5c). Calculated Al-O bond distance (1.77 Å) is longer than the Si-O bond distance (1.65 Å). This is due to the larger ionic radius and smaller charge density of Al^{3+} than that of Si^{4+} .

There is no shift in the Fermi energy upon doping of Ge on the Fe site (refer to Fig. 5f). Very small peaks associated with Ge appear near the Fermi level (refer to Fig. 5g). Metallic behavior is still maintained. A small difference in the Ge-O bond distance (1.91 Å) is noted compared to Fe-O bond distances. This is due to the small difference in the ionic radius and charge mismatch. Constant charge density plot of Ge-doped on the Fe site in $\text{Mg}_3\text{Fe}_2\text{Si}_3\text{O}_{12}$ is shown in Fig. 5h.

4. Conclusions

In the present study, we used classical and DFT simulations to examine the defect, diffusion, dopant and electronic properties of garnet type $\text{Mg}_3\text{Fe}_2\text{Si}_3\text{O}_{12}$. The Mg-Fe anti-site defect cluster is the lowest energy intrinsic defect process. Mg-ion diffusion in this material is three-dimensional with a high activation energy of 2.19 eV and therefore it is low. The Mg, Fe and Si sites prefer to be doped by isovalent Mn^{2+} , Ga^{3+} and Ge^{4+} ions respectively. Capacity of this material can be increased by the formation of additional Mg in the form of interstitials by doping of Al^{3+} on the Si site. The formation of Mg vacancies required for the vacancy assisted migration can be facilitated by the doping of Ge^{4+} on the Fe site. Doping reduced the diffusion barrier only by 0.1 eV suggesting that it would be difficult to make this material suited ion conductor.

Credit authorship contribution statement

Navaratnarajah Kuganathan: Investigation, Data curation, Writing-original draft. Alexander Chroneos: Writing-review & editing.

Funding

This research was financially supported by European Union's H2020 Programme under Grant Agreement no 824072– HARVESTORE.

Declaration of competing interest

The authors declare that they have no known competing financial interests or personal relationships that could have appeared to influence the work reported in this paper.

Acknowledgments

We acknowledge Coventry University and Imperial College London for providing computing facilities.

Appendix A. Supplementary data

Supplementary data to this article can be found online at <https://doi.org/10.1016/j.powera.2020.100016>.

References

- N. Nitta, F. Wu, J.T. Lee, G. Yushin, Li-ion battery materials: present and future, *Mater. Today* 18 (2015) 252–264.
- M. Li, J. Lu, Z. Chen, K. Amine, 30 Years of lithium-ion batteries, *Adv. Mater.* 30 (2018), 1800561.
- T. Kim, W. Song, D.-Y. Son, L.K. Ono, Y. Qi, Lithium-ion batteries: outlook on present, future, and hybridized technologies, *J. Mater. Chem.* 7 (2019) 2942–2964.
- M. Winter, B. Barnett, K. Xu, Before Li ion batteries, *Chem. Rev.* 118 (2018) 11433–11456.
- J.B. Goodenough, K.-S. Park, The Li-ion rechargeable battery: a perspective, *J. Am. Chem. Soc.* 135 (2013) 1167–1176.
- B.L. Ellis, L.F. Nazar, Sodium and sodium-ion energy storage batteries, *Curr. Opin. Solid State Mater. Sci.* 16 (2012) 168–177.
- J.-Y. Hwang, S.-T. Myung, Y.-K. Sun, Sodium-ion batteries: present and future, *Chem. Soc. Rev.* 46 (2017) 3529–3614.
- M. Mao, T. Gao, S. Hou, C. Wang, A critical review of cathodes for rechargeable Mg batteries, *Chem. Soc. Rev.* 47 (2018) 8804–8841.
- R.J. Gummow, G. Vamvounis, M.B. Kannan, Y. He, Calcium-ion batteries: current state-of-the-art and future perspectives, *Adv. Mater.* 30 (2018) 1801702.
- D. Selvakumaran, A. Pan, S. Liang, G. Cao, A review on recent developments and challenges of cathode materials for rechargeable aqueous Zn-ion batteries, *J. Mater. Chem.* 7 (2019) 18209–18236.
- H.D. Yoo, I. Shterenberg, Y. Gofer, G. Gershinsky, N. Pour, D. Aurbach, Mg rechargeable batteries: an on-going challenge, *Energy Environ. Sci.* 6 (2013) 2265–2279.
- Z. Zhao-Karger, M. Fichtner, Beyond intercalation chemistry for rechargeable Mg batteries: a short review and perspective, *Frontiers in Chemistry* 6 (2019).
- J. Bitenc, R. Dominko, Opportunities and challenges in the development of cathode materials for rechargeable Mg batteries, *Frontiers in Chemistry* 6 (2018).
- E. Levi, Y. Gofer, D. Aurbach, On the way to rechargeable Mg batteries: the challenge of new cathode materials, *Chem. Mater.* 22 (2010) 860–868.
- N. Amir, Y. Vestfrid, O. Chusid, Y. Gofer, D. Aurbach, Progress in nonaqueous magnesium electrochemistry, *J. Power Sources* 174 (2007) 1234–1240.
- P. Novák, Electrochemical insertion of magnesium in metal oxides and sulfides from aprotic electrolytes, *J. Electrochem. Soc.* 140 (1993) 140.
- S.A.T. Redfern, G. Artioli, R. Rinaldi, C.M.B. Henderson, K.S. Knight, B.J. Wood, Octahedral cation ordering in olivine at high temperature. II: an in situ neutron powder diffraction study on synthetic MgFeSiO_4 (Fa50), *Phys. Chem. Miner.* 27 (2000) 630–637.
- J. Yin, A.B. Brady, E.S. Takeuchi, A.C. Marschillo, K.J. Takeuchi, Magnesium-ion battery-relevant electrochemistry of MgMn_2O_4 : crystallite size effects and the notable role of electrolyte water content, *Chem. Commun.* 53 (2017) 3665–3668.
- J. Lee, I.D. Seymour, A.J. Pell, S.E. Dutton, C.P. Grey, A systematic study of ^{25}Mg NMR in paramagnetic transition metal oxides: applications to Mg-ion battery materials, *Phys. Chem. Chem. Phys.* 19 (2017) 613–625.
- D.B. Le, S. Passerini, F. Coustier, J. Guo, T. Soderstrom, B.B. Owens, W.H. Smyrl, Intercalation of polyvalent cations into V2O5 aerogels, *Chem. Mater.* 10 (1998) 682–684.
- R. Zhang, X. Yu, K.-W. Nam, C. Ling, T.S. Arthur, W. Song, A.M. Knapp, S.N. Ehrlich, X.-Q. Yang, M. Matsui, $\alpha\text{-MnO}_2$ as a cathode material for rechargeable Mg batteries, *Electrochem. Commun.* 23 (2012) 110–113.
- M.E.A.-d. Dompablo, C. Krich, J. Nava-Avendaño, N. Biškup, M.R. Palacin, F. Bardé, A joint computational and experimental evaluation of CaMn_2O_4 polymorphs as cathode materials for Ca ion batteries, *Chem. Mater.* 28 (2016) 6886–6893.
- J. Heath, H. Chen, M.S. Islam, MgFeSiO_4 as a potential cathode material for magnesium batteries: ion diffusion rates and voltage trends, *J. Mater. Chem.* 5 (2017) 13161–13167.
- A. Torres, F.J. Luque, J. Tortajada, M.E. Arroyo-de Dompablo, Analysis of minerals as electrode materials for Ca-based rechargeable batteries, *Sci. Rep.* 9 (2019) 9644.
- G.A. Novak, G.V. Gibbs, The crystal chemistry of the silicate garnets, *Am. Mineral.* 56 (1971) 791–825.
- N. Kuganathan, A. Kordatos, M.E. Fitzpatrick, R.V. Vovk, A. Chroneos, Defect process and lithium diffusion in Li_2TiO_3 , *Solid State Ionics* 327 (2018) 93–98.
- M.S. Islam, C.A.J. Fisher, Lithium and sodium battery cathode materials: computational insights into voltage, diffusion and nanostructural properties, *Chem. Soc. Rev.* 43 (2014) 185–204.
- N. Kuganathan, A. Chroneos, Defects and dopant properties of $\text{Li}_3\text{V}_2(\text{PO}_4)_3$, *Sci. Rep.* 9 (2019) 333.
- N. Kuganathan, L.H. Tsoukalas, A. Chroneos, Defects, dopants and Li-ion diffusion in Li_2SiO_3 , *Solid State Ionics* 335 (2019) 61–66.
- J.D. Gale, A.L. Rohl, The general utility lattice program (GULP), *Mol. Simulat.* 29 (2003) 291–341.
- J.D. Gale, GULP: a computer program for the symmetry-adapted simulation of solids, *Journal of the Chemical Society, Faraday Trans.* 93 (1997) 629–637.
- N.F. Mott, M.J. Littleton, Conduction in polar crystals. I. Electrolytic conduction in solid salts, *Trans. Faraday Soc.* 34 (1938) 485–499.
- P. Varotsos, Defect volumes and the equation of state in $\alpha\text{-PbF}_2$, *Phys. Rev. B* 76 (2007), 092106.
- P. Varotsos, Comparison of models that interconnect point defect parameters in solids with bulk properties, *J. Appl. Phys.* 101 (2007), 123503.
- A. Chroneos, R.V. Vovk, Modeling self-diffusion in UO_2 and ThO_2 by connecting point defect parameters with bulk properties, *Solid State Ionics* 274 (2015) 1–3.
- M.W.D. Cooper, R.W. Grimes, M.E. Fitzpatrick, A. Chroneos, Modeling oxygen self-diffusion in UO_2 under pressure, *Solid State Ionics* 282 (2015) 26–30.
- G. Kresse, J. Furthmüller, Efficient iterative schemes for ab initio total-energy calculations using a plane-wave basis set, *Phys. Rev. B* 54 (1996) 11169–11186.
- P.E. Blöchl, Projector augmented-wave method, *Phys. Rev. B* 50 (1994) 17953–17979.
- J.P. Perdew, K. Burke, M. Ernzerhof, Generalized gradient approximation made simple, *Phys. Rev. Lett.* 77 (1996) 3865–3868.
- H.J. Monkhorst, J.D. Pack, Special points for Brillouin-zone integrations, *Phys. Rev. B* 13 (1976) 5188–5192.
- S. Grimme, J. Antony, S. Ehrlich, H. Krieg, A consistent and accurate ab initio parametrization of density functional dispersion correction (DFT-D) for the 94 elements H–Pu, *J. Chem. Phys.* 132 (2010), 154104.
- F.A. Kröger, H.J. Vink, Relations between the concentrations of imperfections in crystalline solids, in: F. Seitz, D. Turnbull (Eds.), *Solid State Physics*, Academic Press, 1956, pp. 307–435.
- A.R. Armstrong, N. Kuganathan, M.S. Islam, P.G. Bruce, Structure and lithium transport pathways in $\text{Li}_2\text{FeSiO}_4$ cathodes for lithium batteries, *J. Am. Chem. Soc.* 133 (2011) 13031–13035.
- M. Kempaiah Devaraju, Q. Duc Truong, H. Hyodo, Y. Sasaki, I. Honma, Synthesis, characterization and observation of antisite defects in LiNiPO_4 nanomaterials, *Sci. Rep.* 5 (2015), 11041.
- V.V. Politaev, A.A. Petrenko, V.B. Nalbandyan, B.S. Medvedev, E.S. Shvetsova, Crystal structure, phase relations and electrochemical properties of monoclinic $\text{Li}_2\text{MnSiO}_4$, *J. Solid State Chem.* 180 (2007) 1045–1050.
- C.A.J. Fisher, V.M. Hart Prieto, M.S. Islam, Lithium battery materials LiMPO_4 (M = Mn, Fe, Co, and Ni): insights into defect association, transport mechanisms, and doping behavior, *Chem. Mater.* 20 (2008) 5907–5915.
- S.-i. Nishimura, G. Kobayashi, K. Ohoyama, R. Kanno, M. Yashima, A. Yamada, Experimental visualization of lithium diffusion in Li_xFePO_4 , *Nat. Mater.* 7 (2008) 707.
- N. Kuganathan, K. Davazoglou, A. Chroneos, Computer modeling investigation of MgV_2O_4 for Mg-ion batteries, *J. Appl. Phys.* 127 (2020), 035106.
- N. Kuganathan, P. Iyngaran, R. Vovk, A. Chroneos, Defects, dopants and Mg diffusion in MgTiO_3 , *Sci. Rep.* 9 (2019) 4394.
- N. Kuganathan, E.I. Gkanas, A. Chroneos, Mg_6MnO_8 as a magnesium-ion battery material: defects, dopants and Mg-ion transport, *Energies* 12 (2019) 3213.
- T. Chen, G. Sai Gautam, W. Huang, G. Ceder, First-principles study of the voltage profile and mobility of Mg intercalation in a chromium oxide spinel, *Chem. Mater.* 30 (2018) 153–162.
- C. Ling, F. Mizuno, Phase stability of post-spinel compound AMn_2O_4 (A = Li, Na, or Mg) and its application as a rechargeable battery cathode, *Chem. Mater.* 25 (2013) 3062–3071.
- C. Tealdi, M. Saiful Islam, L. Malavasi, G. Flor, Defect and dopant properties of MgTa_2O_6 , *J. Solid State Chem.* 177 (2004) 4359–4367.
- P. Arunkumar, W.J. Jeong, S. Won, W.B. Im, Improved electrochemical reversibility of over-lithiated layered Li_2RuO_3 cathodes: understanding aliovalent Co^{3+} substitution with excess lithium, *J. Power Sources* 324 (2016) 428–438.